

Research

# Effect of higher H<sub>2</sub>S concentration over CO<sub>2</sub> in acid gas mixtures during geosequestration

Kofi Ofori<sup>1</sup> · Ahmed Barifcani<sup>1</sup> · Chi M. Phan<sup>1</sup>

Received: 22 September 2023 / Accepted: 2 November 2023

Published online: 17 November 2023

© The Author(s) 2023 [OPEN](#)

## Abstract

Decarbonisation of most industrial processes is imperative to achieve climate neutrality. In oil and gas, carbon dioxide (CO<sub>2</sub>) and natural gas are being discovered together with increasingly higher quantities of hydrogen sulphide (H<sub>2</sub>S). The negative effects of acid gases (predominantly CO<sub>2</sub> and H<sub>2</sub>S) in that industry mean they have to be separated before both natural gas and petroleum fuels can be classified as safe for transportation and usage. The separated acid gas, usually composed of a higher CO<sub>2</sub> volume is stored and utilised in enhanced oil recovery (EOR) or geologically stored (geosequestered) in formations. There are increasingly instances in which higher volume of H<sub>2</sub>S acid gas mixtures are being discovered and explored. In this work, the effects of a higher mole percentage H<sub>2</sub>S in an acid gas mixture is investigated using molecular dynamics simulations. The analysis found that it was easier for higher CO<sub>2</sub> acid mixtures to reach pressure convergence comparatively. It has also been discovered that higher H<sub>2</sub>S acid gas mixtures had lower interfacial tension, which makes them more hydrophilic and more miscible with the formation water. The higher H<sub>2</sub>S acid gas content mixtures also have wider water coverage widths and greater interfacial interactivity between the injected and formation fluids. From the density profiles, H<sub>2</sub>S gas in the higher H<sub>2</sub>S acid gas mixture is found to have more influence on the higher H<sub>2</sub>S acid gas/water injection/sequestration process compared to the effect of CO<sub>2</sub> on the higher CO<sub>2</sub> acid gas mixture/water. While H<sub>2</sub>S is slightly more polar than the nonpolar CO<sub>2</sub>, the carbon of CO<sub>2</sub>'s ability to form strong dipole–dipole interactions with the oxygen of water increases the CO<sub>2</sub>'s polarity, and this is reflected in the assertion of the primacy of the O<sub>H<sub>2</sub>O</sub> ⋯ C<sub>CO<sub>2</sub></sub> interaction over all other pairs from the radial distribution function in the water/acid gas mixture during geosequestration. This demonstrates also that a reduction in interfacial tension is possible even for hydrophobic phases.

**Keywords** Geosequestration · Acid gases · Molecular dynamics · Interfacial properties

## Abbreviations

AGRU	Acid gas removal unit
EOR	Enhanced oil recovery
EPM2	Elementary physical model [CO <sub>2</sub> model]
IFT	Interfacial tension
LAMMPS	Large-scale atomic/molecular massively parallel simulator
LJ	Lennard–Jones
MD	Molecular dynamics
MOF	Metal–organic frameworks
MPa	Megapascals
NERD	Nath, Escobedo and de Pablo [H <sub>2</sub> S model]

✉ Kofi Ofori, kofi.ofori@postgrad.curtin.edu.au | <sup>1</sup>Discipline of Chemical Engineering, WASM, Curtin University, Perth, WA 6845, Australia.



Discover Chemical Engineering

(2023) 3:18

| <https://doi.org/10.1007/s43938-023-00035-4>

NpNAT	Constant number of particles, pressure in x and y dimension, x and y area and temperature
NVT	Constant number of particles, volume and temperature
OPLS	Potentials proposed by Jorgensen et al
PPPM	Particle–particle–particle–mesh
RDF	Radial distribution function
TIP4P/2005	Four-site water model

## 1 Introduction

Acid gas—the mixture of the fundamental greenhouse gas CO<sub>2</sub> and the anaerobically produced H<sub>2</sub>S—has always been problematic in natural gas and oil fields. Hitherto, a lot of these fields and reservoirs with high acid gas content were left unexplored but rising usage of fossil fuels [1] means a higher percentage of sour fields are now being given more attention [2, 3]. Prominent examples include the Tengiz and the notorious Kashagan fields in Kazakhstan, both with up to 17% H<sub>2</sub>S and holding the distinction of being the two largest hydrocarbon reserves discovered in some decades. Additionally, two in five unproduced gas reserves are deemed as sour [4], a designation that requires only 4 ppm H<sub>2</sub>S. As demand for natural gas has steadily increased [5] despite the slight blip caused by the pandemic in 2020 [6], it has become progressively imperative to reconsider these acid gas fields. They will be in play for the foreseeable future because;

- Natural gas is a lower CO<sub>2</sub> emitter compared to other fossil fuels [7, 8]
- Green and other ‘clean’ hydrogens and emerging new energy sources have not fully broken through yet,
- The relatively slower advances in the overall clean and renewable energy technologies compared to wholesale demand for energy growth [9],
- And the urgency of secure energy [10] especially in poorer countries [11].

Because of the effects of global warming—due to the aforementioned rise in fossil fuel utilisation, with the year 2022 coinciding with the highest CO<sub>2</sub> emissions from fossil fuel on record at 36.6 billion tonnes [12]—reducing greenhouse gases has become paramount, with methods including looping [13–15] and other reduction technologies to convert CO<sub>2</sub> [16]. Storage of CO<sub>2</sub> in geological receptacles has been identified as the chief management strategy in the effort to combat climate change [17]. The separation of these acid gases from hydrocarbons is essential as both CO<sub>2</sub> and H<sub>2</sub>S are corrosive [18] to equipment, and toxic to humanity and the environment [19] and in the workplace [20] especially in the aqueous form [5]. They also reduce the heating value of natural gas [6]. In addition, the separation of the acid gases is imperative to reach safety [21], sale and transportation benchmarks [22]. Several mechanisms to separate the CO<sub>2</sub>, H<sub>2</sub>S or the acid gas from hydrocarbons are available [23] but research into more efficient means to remove acid gas from some industrial processes still ranks very highly [24]. The five most important separation techniques are through absorption [24], adsorption, distillation, membrane separation processes [25] and through the use of hydrates [26]. Some factors that affect the separation technique selection of choice include the amount of acid gas content in natural gas, viscosity, density and economics [27]. In natural gas separation, absorption is by far the most common method deployed, and selectively absorbing the H<sub>2</sub>S or CO<sub>2</sub> usually uses an aqueous amine or a variant in an acid gas removal unit (AGRU). Ionic liquids with high selectivity for either the H<sub>2</sub>S or CO<sub>2</sub> are also employed in some absorption processes [28], sometimes together with alkanolamines because they are chemically and thermally steady, acid gases dissolve well in them and they are inexpensive as well [29]. Membrane-based separation is proposed as being energy efficient compared to amines though there is a threshold of the individual acid gases’ concentration to make the separation effective [30]. Zeolites and other physical adsorbents such as activated carbon (charcoal) and metal oxides are used for low percentage H<sub>2</sub>S removal [28]. Cryogenic distillation is another such means for separation and has been presented as an alternative to adsorption– and absorption–based products due to less energy and tread required for the large scale removal of undesirable fluids [6]. Metal–organic frameworks (MOFs) are also employed in selective separation [31, 32]. A scheme incorporating both absorption and the hydrate-based separation for high acid gas content has been found to comparatively reduce operating cost [33]. Qayyum et al. [1] provided a systematic listing of various techniques for separating acid gases and other contaminants from natural gas. After separation, the Claus process [34] and its variants like the direct catalytic oxidation [35] can be used to convert the separated H<sub>2</sub>S into elemental sulphur. The Claus process has always been the traditional option, though it is becoming increasingly unviable economically [36], is generally

not adequate as a separation technique in high component CO<sub>2</sub> acid gas mix for sulphur production [37], and the use of direct selective oxidation is on the ascendancy [5]. Because of the global push to achieve net-zero by 2050 whereby the emissions of both anthropological and greenhouse gases from natural processes into the atmosphere is basically cancelled out by the greenhouse gases — mainly carbon or carbon equivalent units — removed from the atmosphere, the question arises as to how the captured CO<sub>2</sub> and by extension the H<sub>2</sub>S can be utilised or environmentally disposed of. Typically, CO<sub>2</sub> has been used in enhanced oil recovery as a tertiary recovery effort but an increased sour concentration may sometimes render that unfeasible due to a lack of facilities and equipment to accommodate and control the more toxic and corrosive H<sub>2</sub>S during the acid gas flooding phase to effectively and efficiently displace some of the residual hydrocarbons [38]. An efficient and increasingly cost-effective means is to permanently store the separated and captured acid gas into geological formations [36, 39] including depleted oil and gas reservoirs and saline aquifers, and also gas hydrate reservoirs and formations [40, 41]. The storage and/or utilisation of captured carbon is seen to be among the best measures to realising net-zero/carbon neutrality and mitigating the effects of climate change [42]. Add to that the presence of high-volume H<sub>2</sub>S and it even lends further credence to store both acid gases together to economically save on costs. Before any geological storage (geosequestration) can take place, an analysis of the security and safety of the injected acid gas must be performed to minimise leakage [43] and ensure long-term containment of the stored gas. Any such analysis involves a wide range of both physical and thermodynamical properties from both fluid–fluid and fluid–fluid–rock interactions, primarily the interfacial tension and contact angles. A knowledge of interfacial properties and phase behaviour is essential in the design of the systems [44] for injection and sequestration. Ideally, the best way to procure these physicochemical properties is directly from formation source or through experiments. But at higher temperatures and pressures, it becomes nearly impossible to perform these experiments or obtain these properties [45], hence an alternate but rigorous and reliable means is required to obtain these parameters. Molecular dynamics (MD) simulation has been proven to be one such theoretical option [46] for collecting and collating data about reservoirs, formations and their characteristics, where data cannot be easily acquired from source, lab tests and experiments [47]. Also, for the interfacial concept which is extensively used in this work, MD presents microscale details that experiments are not capable of affording even under conventional settings [48, 49].

Fluid–fluid and fluid–fluid–rock are the broad factors that affect acid gas geosequestration. This work focuses on the fluid–fluid interactions between the injected acid gas (CO<sub>2</sub> and H<sub>2</sub>S) and the formation water in a depleted oil and gas reservoir. Though most reservoirs have higher CO<sub>2</sub> to H<sub>2</sub>S ratios, and acid gas mixtures usually have a higher mole or volume concentration of CO<sub>2</sub> during injection, there are lots of instances where a higher H<sub>2</sub>S concentration is injected. Machel [50] details one such example where an 85% H<sub>2</sub>S to 15% CO<sub>2</sub> may be injected and could go as high as 95%. Research has shown that in a high mole percentage CO<sub>2</sub> acid gas mixture, the CO<sub>2</sub> is the controlling agent [51] during geosequestration. This work investigates the effects a higher mole percentage H<sub>2</sub>S has on the acid gas mixture and the formation water during geosequestration through some fluid–fluid physicochemical parameters. And with issues being faced by pioneering projects such as Sleipner and Snøhvit [52] wherein the former has injected fluids becoming buoyant, escaping from formation fluids and drifting to just underneath the cap rock and the latter's injection period severely curtailed, this work could potentially aid in a better understanding of molecular interactions during and in the aftermath of geosequestration.

## 2 Computational models and methods

At isothermal conditions of 77 °C and with pressures ranging from 0.5 to 15.6 MPa, MD simulations were carried out using the Large-scale Atomic/Molecular Massively Parallel Simulator (LAMMPS) MD engine [53]. Table 1 shows the model parameters used in this work (Fig. 1).

Water was modelled with TIP4P/2005 [54] because it encapsulates water's phase properties and interfacial properties better than most, and due to its interfacial liquid–vapour parametrisation, CO<sub>2</sub> by the EPM2 [55] was similarly used in this work. Because of uncertainty especially after saturation pressures are reached, two different H<sub>2</sub>S models are used, the NERD [56] and the OPLS [57]. All molecular models comprise three Lennard–Jones sites, with the exception of the TIP4P/2005 model, which contains an auxiliary fourth site, located/bonded at the oxygen atom which allows the model to better capture experimental properties. All models used are also rigid molecules, which have been shown to work reasonably well for low molar weight molecules [58] such as are used in this work. Initially, a 40\*40\*40AA<sup>3</sup>

**Table 1** Force field parameters employed for: water (TIP4P/2005), CO<sub>2</sub> (EPM2) and H<sub>2</sub>S (OPLS and NERD)

	Atom	$\sigma$ (Å)	$\epsilon$ (kcal/mol)	q (e)	Bond	Length (Å)	Angle	$\theta$ (°)
H <sub>2</sub> O	O	3.1589	0.1852	0				
	H	0	0	0.5564	O–H	0.9572	H–O–H	104.52
	M			–1.1128	O–M	0.1546		
CO <sub>2</sub>	C	2.757	0.0559	0.6512				
	O	3.033	0.16	–0.3256	C–O	1.149	O–C–O	180
H <sub>2</sub> S [OPLS]	H	0	0	0.235				
	S	3.7	0.25	–0.47	S–H	1.336	H–S–H	92.07
H <sub>2</sub> S [NERD]	H	0.98	0.0078	0.124				
	S	3.72	0.4968	–0.248	S–H	1.365	H–S–H	91.5

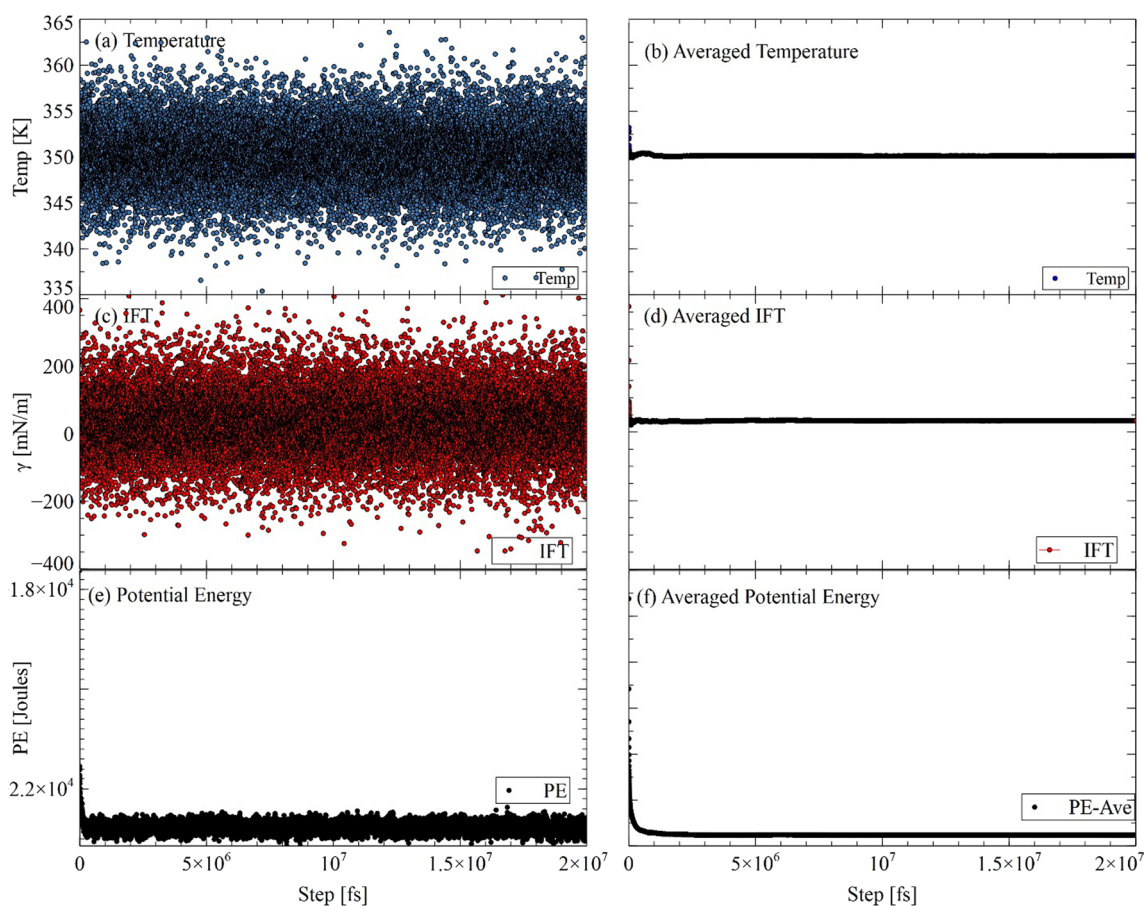
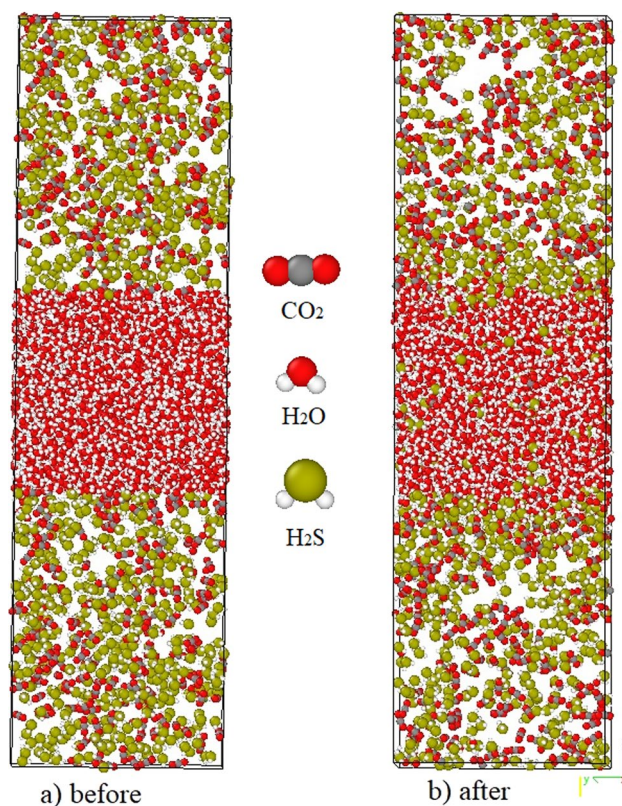


**Fig. 1** Selected parameters as functions of time. **a**, **c** and **e** shows the instantaneous time evolution of selected parameters (temperature, IFT and potential energy) for a 30 mol% CO<sub>2</sub>/70 mol% H<sub>2</sub>S–OPLS system with 1964 water molecules at 15.6 MPa. **b**, **d**, **f** display the time averages of the selected parameters respectively. MD is built on the premise of the ergodic hypothesis, whereby the ensemble average is equivalent to the time average, assuming the time average is calculated during an equilibrium state. In the time average, it is demonstrable that ~2–3 ns is where equilibrium starts but for our purposes, a higher threshold of 5 ns was imposed

box was constructed for both the acid gas and water respectively in the  $Np_NAT$  ensemble, with the tacit allowance for only movement (expansion or contraction) in the  $z$ -dimension, with all other ensemble parameters kept constant (number of molecules, normal pressure,  $x$ - and  $y$ -dimensions, and system temperature). This  $Np_NAT$  simulation was conducted for 2 ns with the first 0.5 ns used as equilibration and the 1.5 ns after for production steps. Once average  $z$ -lengths for both acid gas and water were acquired from the  $Np_NAT$  ensemble simulation, both water and acid gas

**Fig. 2** Snapshots of before and after simulation boxes. above shows a before and after simulation captured at 77 °C and 15.6 MPa with 1964 water molecules in the centre shoehorned between two slabs of high H<sub>2</sub>S acid gas mixture each containing 189 CO<sub>2</sub> molecules and 441 H<sub>2</sub>S molecules. The after shows a smattering of acid gas being absorbed into the water stream while the water's coverage area also widens



were coalesced together with the water slab in the middle sandwiched between two clusters of acid gas Fig. 2(a), with the modified  $z$ -length the sum of the new water and twice the new acid gas  $z$ -lengths.

This composite, which is a box of size  $40 * 40 * (\text{Modified } z) \text{ \AA}^3$  was then run in the  $NVT$  ensemble for 20 ns, the first 5 ns for equilibration and the final 15 ns for production from which analysis is undertaken Fig. 2(b). In all three dimensions, periodic boundary conditions were employed to remove artifacts. Both  $Np_NAT$ , and  $NVT$  (constant number of particles, volume and temperature) used a timestep of 1.0 fs and the Newtonian equations of motion were integrated using the Velocity Verlet algorithm. The dispersive Lennard–Jones (LJ) 12–6 and the electrostatic long-range Coulombics were modelled with the combined equation;

$$\phi_{ij}(r_{ij}) = 4\epsilon_{ij} \left[ \left( \frac{\sigma_{ij}}{r_{ij}} \right)^{12} - \left( \frac{\sigma_{ij}}{r_{ij}} \right)^6 \right] + \frac{q_i q_j}{4\pi\epsilon_0 r_{ij}} \quad (1)$$

where  $\epsilon_{ij}$  represents the interaction energy depth between the pair particles  $i$  and  $j$ ,  $\sigma_{ij}$  is the distance between the particle pair  $i$  and  $j$  when their LJ potential energy is zero,  $r_{ij}$  is the interacting distance between the pair particles  $i$  and  $j$ ,  $q$  is the point charge and  $\epsilon_0$  is the vacuum permittivity. Nonbonded interactions' cutoff distance was set for both LJ and long-range coulombics at 12 Å. The Nose–Hoover thermostat [59, 60] was used to constrain temperatures at the isothermic 77 °C (350 K) and barostat for each of the individual pressures as well. The LJ parameters for nonbonded pairwise unlike atomic interactions were rendered using the Lorentz–Berthelot mixing rules [61]. Long-range electrostatic interactions for the  $Np_NAT$  ensemble were modelled with Ewald summations [62] whereas the particle–particle–particle-mesh (PPPM) [63], a slightly less accurate but computationally an economical method was used for the longer  $NVT$  ensemble runs. Both Ewald sums and PPPM had a relative error of  $10^{-5}$  kcal/mol. All bonds and angles with the exception of the 180° O–C–O angle were constrained with the SHAKE algorithm [64]. A high angle-breaking constant was applied to the O–C–O angle instead to avoid errors introduced by the SHAKE algorithm on straight line angles [65].

### 3 Results and discussion

#### 3.1 Acid gas simulation process controls

These metrics serve to reassure that the simulations are being performed in the right manner. The pure acid gas simulations were rendered in the  $Np_NAT$  ensemble at a constant temperature (77 °C) and over fourteen pressures ranging from 0.5 to 15.6 MPa. They were then compared to NIST experimental and state-of-the-art equations [66]. Fig. 3(a) and (b) show the convergence of the total pressure and z-directional pressures respectively to the NIST baselines. It is evident that the lower pressures have very low standard deviations, or very little fluctuations from the pressure ideal. As pressures increase, and especially after both H<sub>2</sub>S and CO<sub>2</sub> change phase, the pressure oscillations increase. This is more so for the higher H<sub>2</sub>S acid gas mixtures, especially the NERD model. Conversely, the temperature reaches convergence easily at the higher pressures Fig. 3(c), (d) is not a simulation control but a measure of the average size of the fluctuating z-dimension and its impact on the simulation dynamics. Crucially, all size lengths are within an error bar of each other before phase change occurs. Then, after phase change, in a like-for-like model, higher CO<sub>2</sub> to higher H<sub>2</sub>S acid gas mixture comparison (70 mol% CO<sub>2</sub>/30 mol% H<sub>2</sub>S–NERD model compared to 30 mol% CO<sub>2</sub>/70 mol% H<sub>2</sub>S–NERD and 70 mol% CO<sub>2</sub>/30 mol% H<sub>2</sub>S–OPLS model compared to 30 mol% CO<sub>2</sub>/70 mol% H<sub>2</sub>S–OPLS), the higher CO<sub>2</sub> acid gas mixture has a greater length, hence volume. This is due to the force field parametrisation issue alluded to in a prior section of this work, which is magnified especially after components reach saturation pressures.

#### 3.2 IFT

The simulation interfacial tension,  $\gamma$ , was calculated from the Kirkwood-Buff equation [67] as both a function of z-length and simulation time thus;

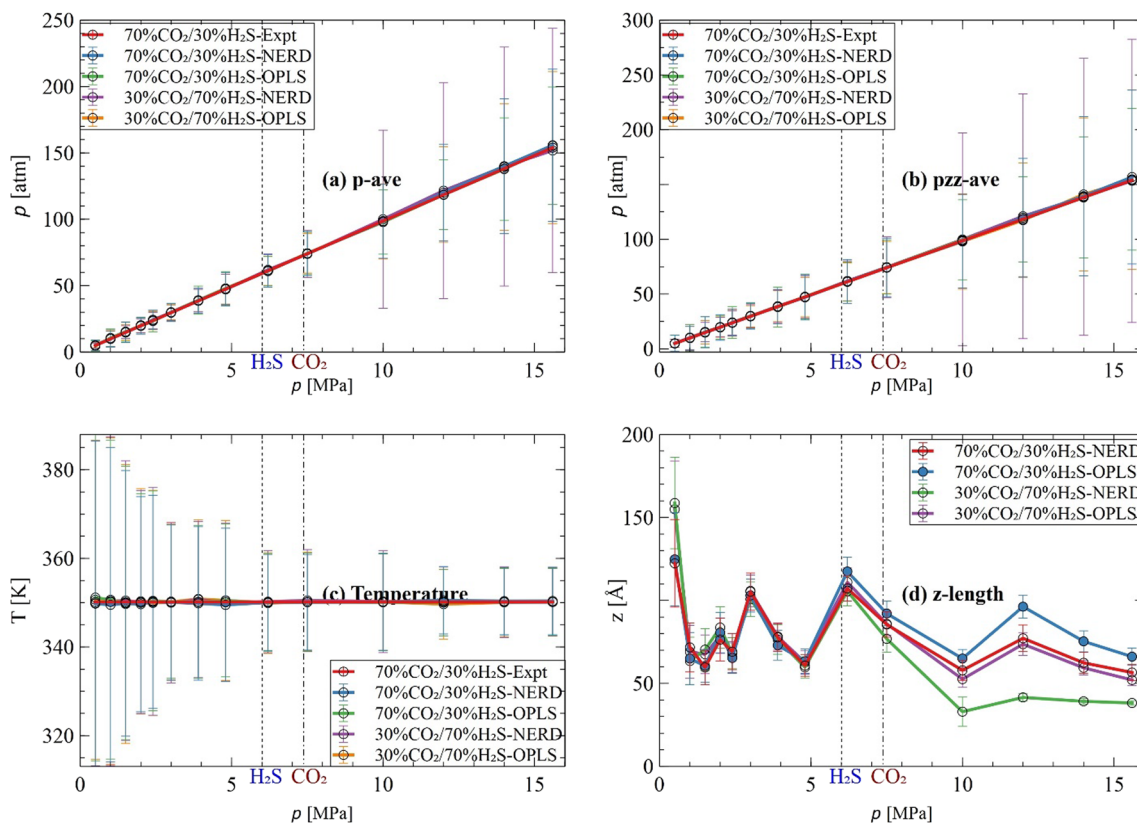


**Fig. 3** Process controls. above shows initial simulations of the acid gas conducted in the  $Np_NAT$  ensemble. **a** system pressure. **b** normal pressure. **c** system temperature and **d** length of  $z$ ,  $L_z$ . At 77 °C, H<sub>2</sub>S changes phase from gas to liquid at 6.01 MPa and CO<sub>2</sub> changes from a gas to a supercritical fluid at 7.38 MPa

$$\gamma(L_z, t) = \frac{1}{n} \int_0^{L_z} \left( p_{zz}(z) - \frac{p_{xx}(z) + p_{yy}(z)}{2} \right) dz \quad (2)$$

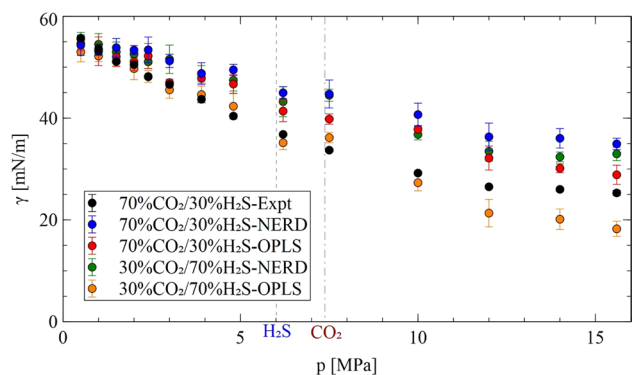
For which  $p_{xx}(z)$ ,  $p_{yy}(z)$  and  $p_{zz}(z)$  represent the pressure components in the stated dimensions and all are functionally dependent on the  $z$ -dimension,  $n$  is the number interfaces—two—and  $L_z$  is the length of the  $z$ -dimension. These calculations were carried out from the  $NVT$  ensemble which incorporated both water and the acid gas mixture. At low pressures, both injected fluids are gases but as pressures increase, phases change and the injected fluids become denser. This increase in density serves to reduce the IFT as an increase in the concentration of the injected fluid results in a decrease in the IFT [68]. This has been attributed to the increased interface roughness resulting from increased fluid mobility due to the increased mass concentration of the injected fluids resulting in a more profound impact at the interface of injected fluids [69], which is in agreement with Le Chatelier's principle. Comparing the two simulated 70 mol%  $\text{CO}_2$ /30 mol%  $\text{H}_2\text{S}$  models to the experimental 70 mol%  $\text{CO}_2$ /30 mol%  $\text{H}_2\text{S}$  values [70] as shown in Fig. 4, it is clear that both simulated models diverge from the experimental data, especially after both  $\text{H}_2\text{S}$  and  $\text{CO}_2$  change phase. This usually is due to parametrisation not taking into account certain atomic/molecular properties [71] or because as parametrisation usually is done for an atom or molecule in a vacuum, the combination of different molecules in a binary or ternary mixtures usually exposes the shortcomings in the individual potential parameters. The employment of rigid models could also have a limiting effect due to the fused momentum of atoms and/or molecules, and this is more noteworthy once molecules reach saturation pressures and results diverge from experimental values as shown in this work. But they are still preferred to flexible models, which while not passing over the atomic/molecular geometrical flexibility, could increase computational processing up to four times [72] and have also been classified as being more trouble than they're worth [73]. Perhaps MD biggest drawback may be its inability to incorporate quantum and electronic effects into molecular interactions but it is still reasonably appropriate when applied to simple fluids and physical systems such as used in this work. Cut-off lengths may also influence other pressure-derived quantities [74]. However, using a like-for-like model comparison, both 30 mol%  $\text{CO}_2$ /70 mol%  $\text{H}_2\text{S}$  simulated values estimate lower IFTs than the 70 mol%  $\text{CO}_2$ /30 mol%  $\text{H}_2\text{S}$ . The lower IFT values indicate that the higher  $\text{H}_2\text{S}$  acid gas mixture is more amenable to being miscible with the formation fluids than the higher  $\text{CO}_2$  acid gas mixture [75]. In other words, the higher the  $\text{H}_2\text{S}$  content, the more hydrophilic the acid gas mixture becomes since  $\text{H}_2\text{S}$  is only slightly more polar than  $\text{CO}_2$ , which is nonpolar, and the more polar a surface is, the more hydrophilic it is [76]. It also is possible for hydrophobic surfaces to have a reduced IFT when their polarity increases [77]. This lowered IFT in high  $\text{H}_2\text{S}$  acid gas mixture is also in agreement with the literature [70].

### 3.3 Density profiles, interfacial thickness

The Gibbs adsorption isotherm is used, which in spite of its shortcomings for certain fluids [78], still figures prominently in interfacial research. Two density profiles were calculated. The first Fig. 5) involved fitting the water density profile to the hyperbolic tangent function [79];

$$\rho(z) = \frac{\rho_l + \rho_v}{2} - \frac{\rho_l - \rho_v}{2} \tanh \left[ \frac{2(z - z_0)}{\delta} \right] \quad (3)$$

**Fig. 4** Comparative interfacial tensions. above shows interfacial tension calculated at 77 °C from the  $NVT$  ensemble for the different model combinations and compared to experimental values, for which only the higher  $\text{CO}_2$  acid mixture data are available. At 77 °C,  $\text{H}_2\text{S}$  changes phase from gas to liquid at 6.01 MPa and  $\text{CO}_2$  changes from a gas to a supercritical fluid at 7.38 MPa



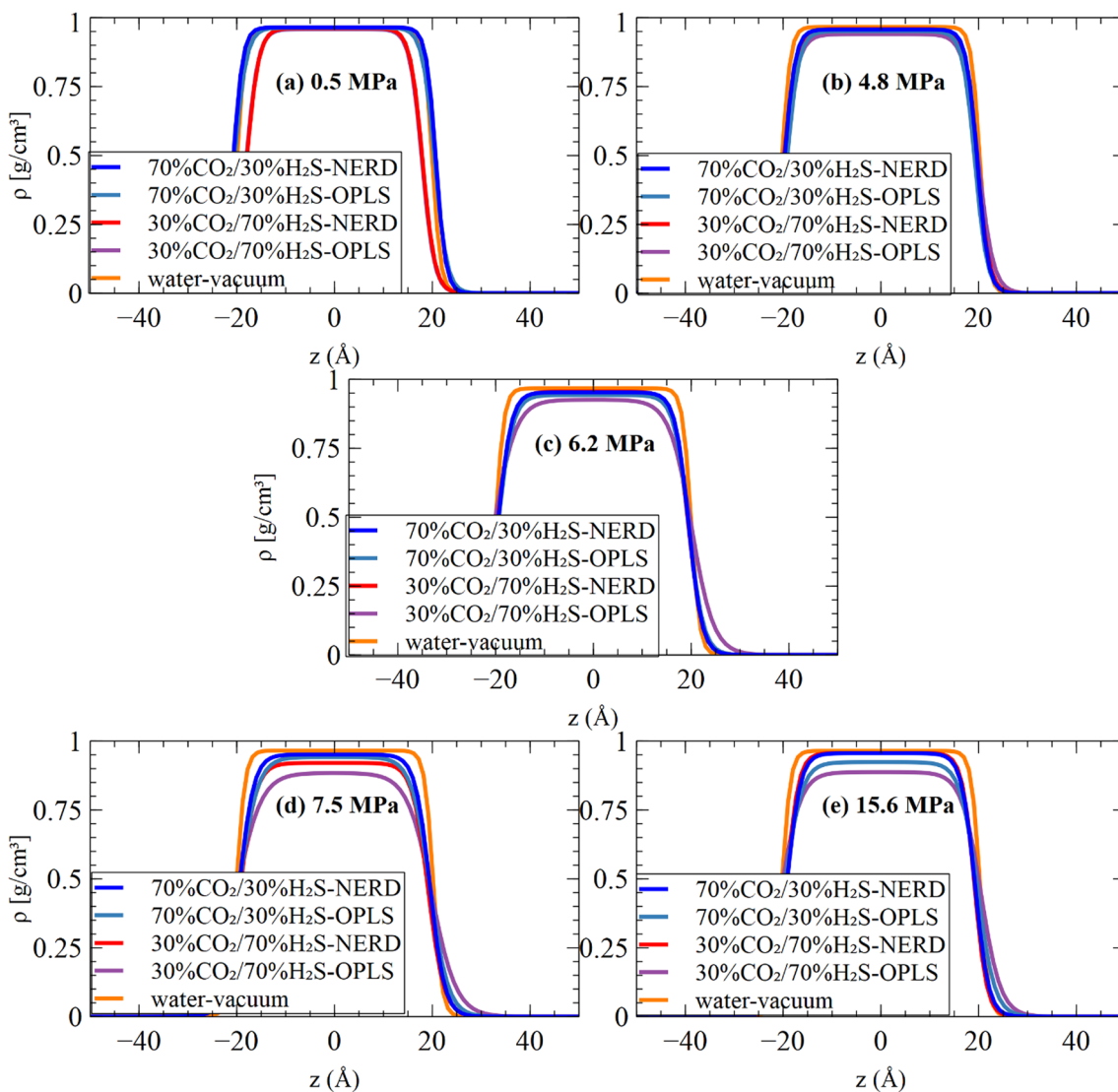


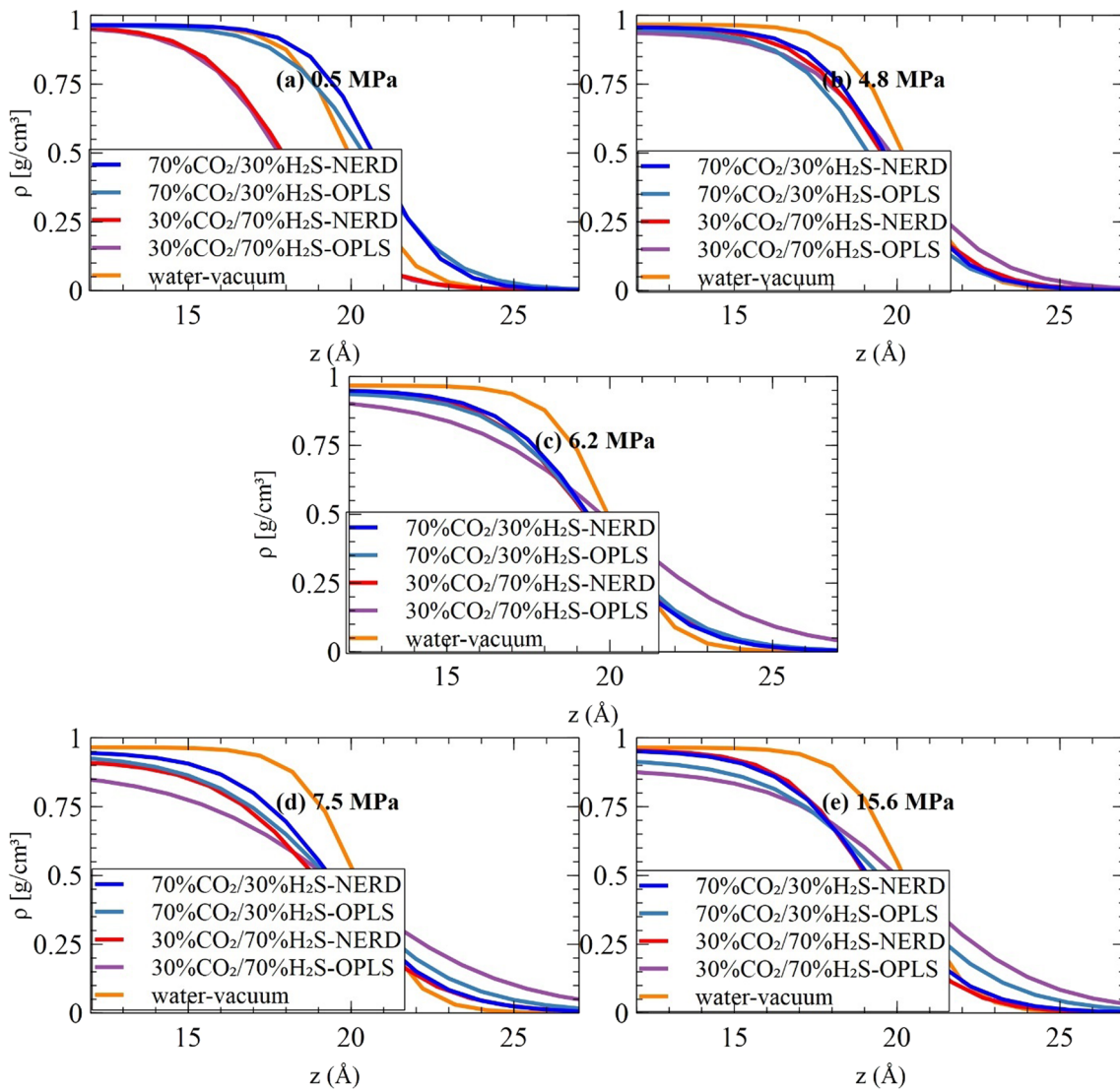
**Fig. 5** Centre-of-mass density profiles. above shows density profiles calculated from the *NVT* ensemble using the hyperbolic tangent function for the formation water at 77 °C and compared to simulated water/vacuum system using the centre-of-mass slant

For which the  $\rho_l$  and  $\rho_v$  are the liquid and vapour phase densities respectively, the interfacial thickness of the Gibbs adsorption isotherm is represented by  $\delta$  and Gibbs dividing plane which is normal to the interface is  $z_0$ . Density distributions were calculated by splitting the  $z$ -dimension into small, 1 Å bins. Pure water and its vacuum were simulated and compared to both cases of higher  $\text{CO}_2$  and higher  $\text{H}_2\text{S}$  acid gas mixtures. In all the five pressure instances, from 0.5 to 15.6 MPa, the water/vacuum simulation showed a much higher density, especially at the higher pressures. The lesser water density in the non-[water/vacuum] simulations is due to the absorption of some of the water into the acid gas stream. Figure 6 shows a much closer look at the profiles. At 0.5 MPa, the two higher  $\text{H}_2\text{S}$  acid gas mixtures have the smallest water coverage widths. The 4.8 MPa does not show any difference between all simulated mixtures. From 6.2 MPa onwards—when phase changes kick in—it is clear that the simulated water has the lowest interfacial thickness, but that the 30 mol%  $\text{CO}_2$ /70 mol%  $\text{H}_2\text{S}$ –OPLS model exhibits a wider thickness which indicates a much larger acid gas coverage at the water interface, hence more interactivity with the formation fluids.

As other studies have shown, the wider the interfacial coverage area, the lower the IFT [51]. Figure 7 also demonstrates that the 30 mol%  $\text{CO}_2$ /70 mol%  $\text{H}_2\text{S}$ –OPLS has a much higher interactivity with the formation fluids than the other models/simulations.

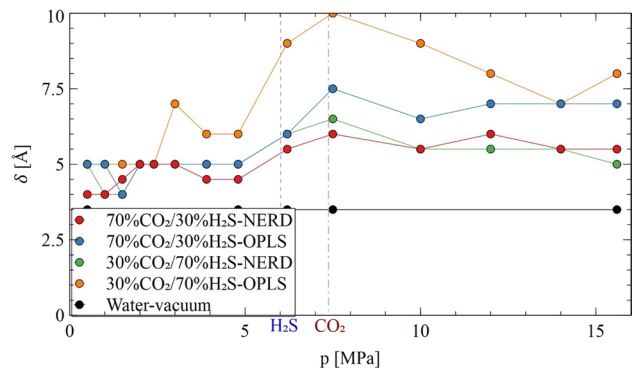
A look at the raw, unfitted density profiles for both water and the acid gas (Fig. 8) shows that the model densities are all very similar except for the highest pressure, 15.6 MPa. The 30 mol%  $\text{CO}_2$ /70 mol%  $\text{H}_2\text{S}$ –NERD shows a much denser





**Fig. 6** Right-of-centre-mass density profiles. shows an in-depth look from the right-of-centre-mass at the density profiles calculated from the NVT ensemble for the formation water at 77 °C and compared to simulated water/vacuum system using the centre-of-mass approach

**Fig. 7** Interfacial thicknesses for the water/acid gas interface. above shows an overview of calculated interfacial thicknesses from the NVT ensemble for the water/acid gas interface at 77 °C compared to simulated water/vacuum system. At 77 °C, H<sub>2</sub>S changes phase from gas to liquid at 6.01 MPa and CO<sub>2</sub> changes from a gas to a supercritical fluid at 7.38 MPa



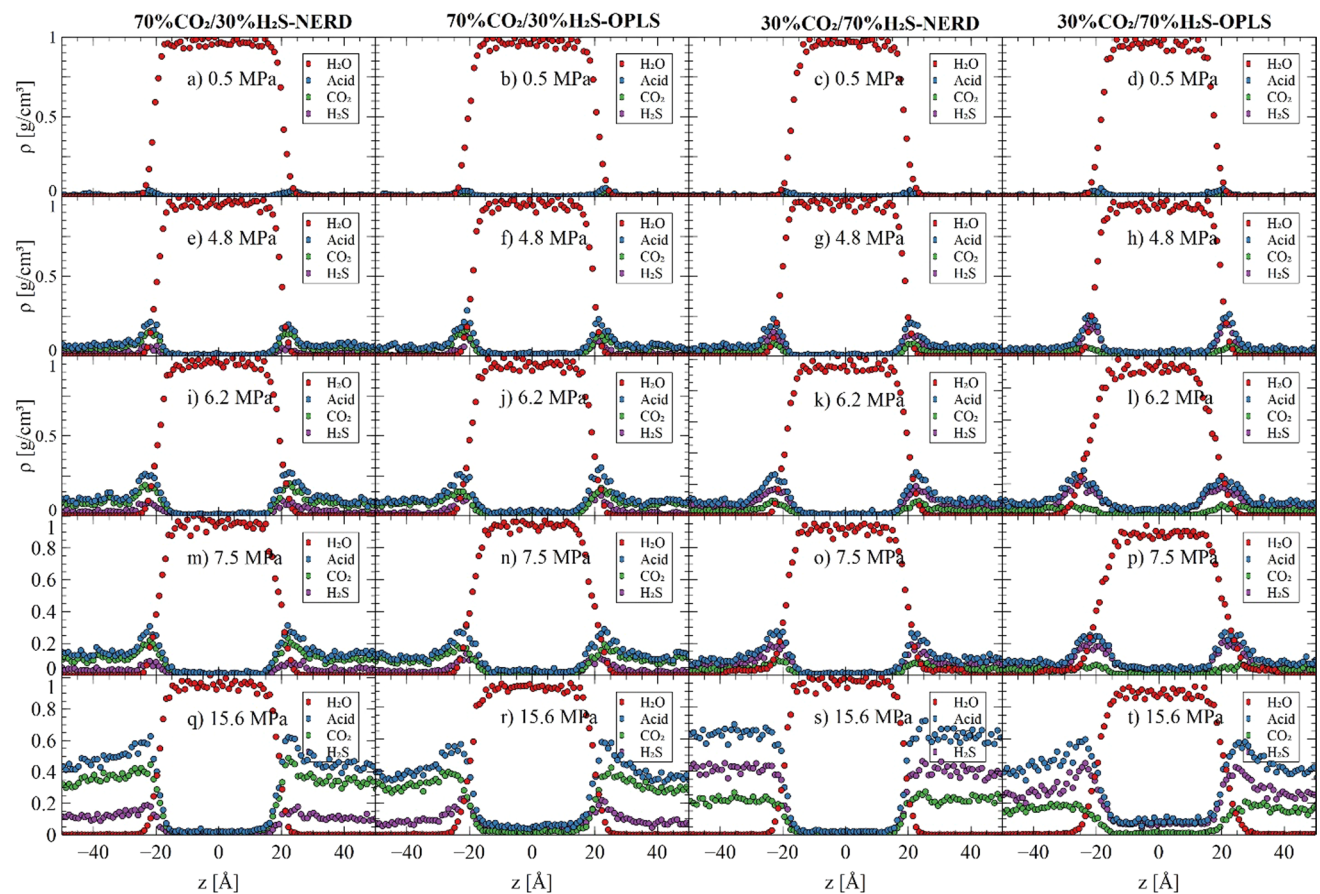


**Fig. 8** Raw, unfitted density profiles calculated from the NVT ensemble for the water, acid gas, and acid gas constituents ( $\text{CO}_2$  and  $\text{H}_2\text{S}$ ) using the centre-of-mass outlook

acid gas compared to all other simulations. The lack of a genuine progression in the 30 mol%  $\text{CO}_2$ /70 mol%  $\text{H}_2\text{S}$ -NERD density from earlier, lower pressure simulations all the way to the 15.6 MPa makes the sudden spike at 15.6 MPa look like an outlier.

### 3.4 Density

A density analysis was also carried out to better understand the effects of the individual molecules—water,  $\text{CO}_2$  and  $\text{H}_2\text{S}$ —involved. Figure 9(a) shows the  $Np_NAT$  simulation of the acid gas. All four simulations are within an error bar of each other at low pressures until after 7.5 MPa, at which point both injected fluids would have changed phase. The 30 mol%  $\text{CO}_2$ /70 mol%  $\text{H}_2\text{S}$ -NERD model strongly diverges and increases steeply in density, much further removed from the other three. In a like-for-like model comparison, it is important to note that the higher  $\text{H}_2\text{S}$  acid gas OPLS model (30 mol%  $\text{CO}_2$ /70 mol%  $\text{H}_2\text{S}$ -OPLS) has a higher density after 7.5 MPa compared to the higher  $\text{CO}_2$  acid gas OPLS model (70 mol%  $\text{CO}_2$ /30 mol%  $\text{H}_2\text{S}$ -OPLS). Because acid gas geosequestration is usually carried out at temperatures and pressures aligned with the compressed gas's transportation conditions [80], the higher density has crucial implications especially in supercritical conditions for which we make observations from the simulations. Figure 9(b) shows the four NVT simulations of the water-acid gas combination against water. The higher  $\text{H}_2\text{S}$  acid gas mixture NERD model displays a higher density compared to all others once again. As alluded to earlier, this looks more like an outlier especially when compared to the experimental values and can be pinned as a model parametrisation issue. But the most important takeaway is that both higher  $\text{H}_2\text{S}$  acid gas mixture models are denser than their higher  $\text{CO}_2$  acid gas mixture counterparts. A breakdown of the individual contributions of the acid gas constituent components in Figure 9(c) and (d) is revealing, demonstrating the predominance of the 30 mol%  $\text{CO}_2$ /70 mol%  $\text{H}_2\text{S}$ -NERD model and its effects on the overall simulation. Figure 9(e) is a validation simulation for the TIP4P/2005 water used in this work and Figure 9(f) shows the water level after NVT simulation. The main observation here is that the higher  $\text{H}_2\text{S}$  acid gas

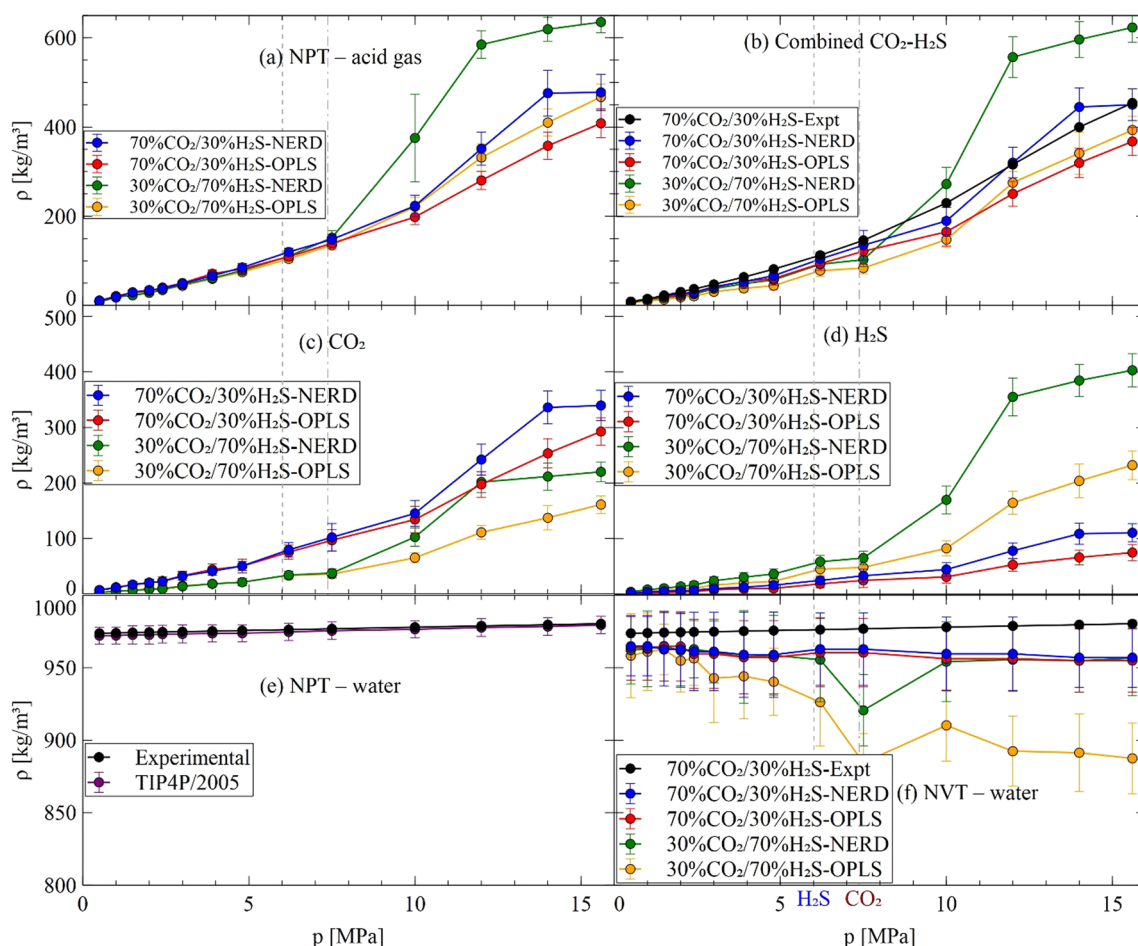


**Fig. 9** Different component densities. above shows densities for various constituent molecular components calculated at 77 °C over wide ranging pressures. **a** the  $Np_NAT$  ensemble simulation of only the acid gas. **b** a comparison of both higher  $\text{CO}_2$  and higher  $\text{H}_2\text{S}$  acid gas mixtures to a higher  $\text{CO}_2$  experimental [70] acid gas mixture from the water/acid gas  $NVT$  ensemble simulation. **c** the effect of the constituent  $\text{CO}_2$  in both higher and lower  $\text{H}_2\text{S}$  acid gas mixtures from water/acid gas  $NVT$  ensemble simulation. **d** the effect of the constituent  $\text{H}_2\text{S}$  in both higher and lower  $\text{H}_2\text{S}$  acid gas mixtures from water/acid gas  $NVT$  ensemble simulation. **e** a validation run in the  $Np_NAT$  ensemble for the TIP4P/2005 water model compared to experimental [70]. **f** the effects of the acid gas on water after  $NVT$  ensemble simulation. At 77 °C,  $\text{H}_2\text{S}$  changes phase from gas to liquid at 6.01 MPa and  $\text{CO}_2$  changes from a gas to a supercritical fluid at 7.38 MPa

mixture models have the lowest water densities. This is due to a predisposition towards more interactivity between the water and the higher  $\text{H}_2\text{S}$  acid gas mixture molecules, as shown by the wider interfacial thickness and coverage area in Fig. 7 and their tendency towards being more miscible/being absorbed into the water stream.

### 3.5 RDF

The radial distribution function (RDF) is practical for revealing insights into the structure of the sequestered fluids in the presence of formation water. It is calculated by the formula;

$$n_{AB} = \int_r^{r+dr} 4\pi\rho_B r^2 g_{AB}(r) dr \quad (4)$$

where  $n_{AB}$  represents the number of  $B$  entities packed around the target  $A$  entity in the distance  $dr$ ,  $g_{AB}(r)$  is the pair distribution function as a function of radial distance and the number density of entity  $B$  is  $\rho_B$ .

The ability to form dipole–dipole interactions, including hydrogen bonding, can alter the polarity of a molecule [82] and this is what happens in this context.  $\text{CO}_2$ , a nonpolar molecule, through the carbon atom's interaction with the highly electronegative oxygen atom of water, is the dominant interaction during the acid gas injection/sequestration process

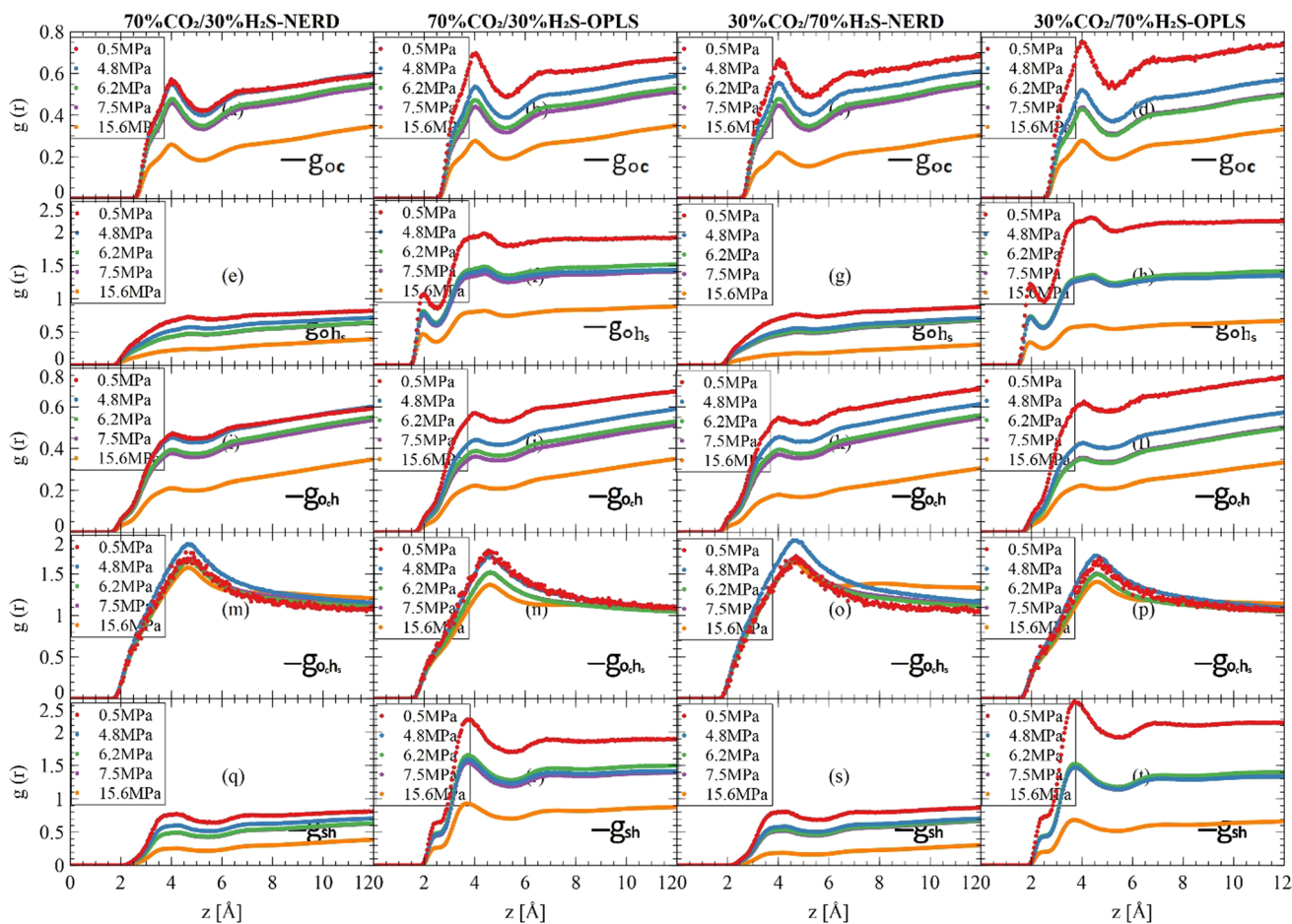
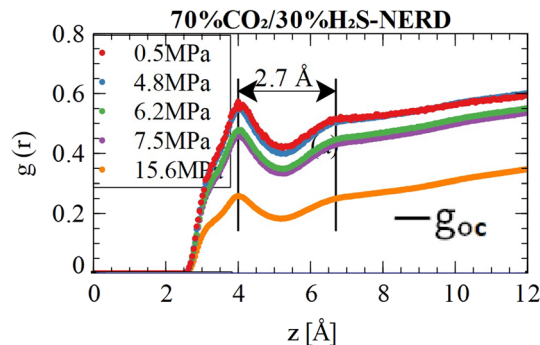


**Fig. 10** The distribution for five different pair functions of pressures above shows the distribution for five different pair functions [ $g_{oc}(r)$ ,  $g_{oh_s}(r)$ ,  $g_{oh}(r)$ ,  $g_{oh_s}(r)$  and  $g_{sh}(r)$ ] as functions of the five focal pressures at 77 °C. **a** to **d** show the  $g_{oc}$  function, which is a relationship between  $O_{H_2O} \cdots C_{CO_2}$ . All four cases demonstrate very strong dipole–dipole interactions, akin to the main dipole–dipole force, hydrogen bonding, which is represented by a well-built first peak. The peaks get stronger with increasing pressures as lower gas levels associated with increasing pressure reduces the associated ‘noise’. Another measure of the strength of the hydrogen bonding is through the distance between the first and second hydration shells. Analyses of all the four  $g_{oc}$  lengths Fig. 11) show that they measure  $\sim 2.7$  Å, which is right at the beginning of the typical hydrogen bond length range of 2.7–3.3 Å [81]

as the other RDF functions have very little or no dipole–dipole interactions at all. In fact, the  $O_{H_2O} \cdots H_{H_2S}$  interaction, represented by the pair function  $g_{oh_s}$  in Fig. 10(e) to (h) shows some hydrogen bonding tendencies especially in the short but demonstrably visible first peaks of the OPLS models, which then proceed to plateau in the second hydration shell. The NERD models have ostensibly lower peaks than the OPLS. Comparably lower/shorter peaks are produced

**Fig. 11** Strong dipole–dipole interactions, mimicking hydrogen bonding between oxygen of water and carbon of  $CO_2$ . Above gives a closer look and measurement of the strong dipole–dipole forces prevalent among all four  $g_{oc}(r)$  pair distribution functions, which represent the interaction between  $O_{H_2O} \cdots C_{CO_2}$



by associated higher orbital/hydration shell energies. The  $g_{o_c h}$  function Fig. 10(i) to (l) of the  $O_{CO_2} \cdots H_{H_2O}$  interaction is uniform all through and similarly, has hydrogen bonding length as the  $O_{H_2O} \cdots C_{CO_2}$ , but not as strong a first peak.  $g_{o_c h_s}$  of the  $O_{CO_2} \cdots H_{H_2S}$  interaction Figure 10(m) to (p) shows a strong first peak associated with strong hydrogen bonding but the absence of a second hydration shell and the disintegration/deceleration to unity of the pair distribution function is prototypical real gas behaviour. The  $S_{H_2S} \cdots LH_{H_2O}$  interactions are conveyed by the  $g_{sh}$  function Figure. 10(q) to (t). Both OPLS and NERD models resolve the interactions differently. Whereas the NERD model is shorter, flatter and broader at both first ( $\sim 4 \text{ \AA}$ ) and second ( $\sim 6.7 \text{ \AA}$ ) hydration shells, the OPLS model's first peak is a shoulder ( $\sim 2.5 \text{ \AA}$ ). Devoid of this shoulder, both possess the hydrogen bonding tendencies we have come to associate with most of the interactions.

## 4 Conclusion

Acid gases—predominantly  $CO_2$  and  $H_2S$ —are problematic in many industries especially in oil and gas. Due to their negative effects, it is imperative that they be separated from the hydrocarbons. After separation, the acid gas mixture, which for the most part contains more  $CO_2$  than  $H_2S$ , is either utilised in processes such as enhanced oil recovery (EOR), or geologically stored (geosequestered). But as more sour reservoirs are discovered and explored, it becomes important to understand the effects a higher  $H_2S$  acid gas mixture will have during the injection and geosequestration process into the depleted oil and gas reservoirs. However, due to reservoir and formation conditions not being ideal for obtaining data first-hand, there is the need to apply an alternative but reliable means to secure data from geosequestration process. To that end, we performed molecular dynamics simulations to investigate key fluid–fluid parameters such as interfacial tension, interfacial thickness, absorption and adsorption, density and radial distribution function. The analyses found that it is harder for pressures in the higher  $H_2S$  acid gas mixture models to converge in the  $Np_N AT$  ensemble, and that the higher  $CO_2$  acid gas mixture has greater volume comparatively. Furthermore, while interfacial tensions diverged from experimental values especially at high pressures after phase change, in general, the higher  $H_2S$  acid gas mixture has lower interfacial tension relatively, hence it is more hydrophilic compared to the higher  $CO_2$  acid gas mixture and ideally better suited to mix or be absorbed into the formation water stream. From the density and density profiles, the higher  $H_2S$  acid gas mixture also shows a higher interactivity with the formation fluids as shown by wider water coverage width and greater interfacial thickness. While a breakdown of the constituent acid gases' density reveals the outsize influence of  $H_2S$  on the higher  $H_2S$  acid gas mixture compared to  $CO_2$ 's influence on the higher  $CO_2$  acid gas mixture, an examination of the radial distribution function demonstrates that the interaction between the oxygen of water and carbon is the strongest among all pairs and this is due to the strong electronegativity of the oxygen atom leading to strong dipole–dipole interactions very similar to hydrogen bonding between them. For benchmarking purposes, the OPLS  $H_2S$  model appears to be a better fit for simulation purposes, showing IFTs closer to the experimental values, wider interfacial coverage area which results in a lower interactive density compared to the NERD model. In regard to the ongoing complications at both Sleipner and Snøhvit, this work sheds light on some of the subterranean fluid–fluid interactions and could potentially help in the management of acid gas injection operations in particular and fluid geosequestrations at large.

**Acknowledgements** Author Kofi Ofori would like to thank the Pawsey Supercomputing Centre for the provision of supercomputing time and resources. This work is dedicated to the memory of Assoc. Prof. Ahmed Barifcani, a co-author, who passed on late August 2023.

**Author contributions** KO: Conceptualisation, Methodology, Visualisation, Writing—original draft and editing; AB: Supervision, Visualisation, Writing—review and editing; CMP: Conceptualisation, Supervision, Writing—review and editing.

**Funding** Not applicable.

**Data Availability** The data that support the findings of this study are available upon reasonable request from the authors.

## Declarations

**Ethics approval and consent to participate** Not applicable.

**Consent for publication** Not applicable.

**Competing interests** The authors have no competing interests to declare that are relevant to the content of this article.

**Open Access** This article is licensed under a Creative Commons Attribution 4.0 International License, which permits use, sharing, adaptation, distribution and reproduction in any medium or format, as long as you give appropriate credit to the original author(s) and the source, provide a link to the Creative Commons licence, and indicate if changes were made. The images or other third party material in this article are included in the article's Creative Commons licence, unless indicated otherwise in a credit line to the material. If material is not included in the article's Creative Commons licence and your intended use is not permitted by statutory regulation or exceeds the permitted use, you will need to obtain permission directly from the copyright holder. To view a copy of this licence, visit <http://creativecommons.org/licenses/by/4.0/>.

## References

1. Qayyum A, Ali U, Ramzan N. Acid gas removal techniques for syngas, natural gas, and biogas clean up—a review. *Energy Sources Part A Recov Utilization Environ Effects*. 2020. <https://doi.org/10.1080/15567036.2020.1800866>.
2. Pellegrini LA, et al. New solvents for CO<sub>2</sub> and H<sub>2</sub>S removal from gaseous streams. *Energies*. 2021;14(20):6687.
3. Ahmad Mubashir, M., et al. Sour Gas Well Testing Challenges-A Successful Case Study in Abu Dhabi International Petroleum Exhibition & Conference. 2019.
4. Lallemand, F., F. Lecomte, and C. Streicher. Highly Sour Gas Processing: H<sub>2</sub>S Bulk Removal With the Sprex Process in International Petroleum Technology Conference. 2005.
5. Spatolisano E, de Angelis AR, Pellegrini LA. Middle scale hydrogen sulphide conversion and valorisation technologies: a review. *ChemBioEng Rev*. 2022;9(4):370–92.
6. Tengku Hassan TNA, et al. Insights on cryogenic distillation technology for simultaneous CO<sub>2</sub> and H<sub>2</sub>S removal for sour gas fields. *Molecules*. 2022;27(4):1424.
7. Srinivasan S. Fuel cells: from fundamentals to applications. Berlin: Springer; 2006.
8. Ma Y, et al. Hydrogen sulfide removal from natural gas using membrane technology: a review. *J Mater Chem A*. 2021;9(36):20211–40.
9. Askarova A, et al. An overview of geological CO<sub>2</sub> sequestration in oil and gas reservoirs. *Energies*. 2023;16(6):2821.
10. Shafiq H, Azam SU, Hussain A. Steam gasification of municipal solid waste for hydrogen production using Aspen Plus® simulation. *Discov Chem Eng*. 2021;1(1):4.
11. Halkos G, Gkampoura E-C. Assessing fossil fuels and renewables—impact on energy poverty conditions in Europe. *Energies*. 2023;16(1):560.
12. Friedlingstein P, et al. Global carbon budget 2022. *Earth Syst Sci Data*. 2022;14(11):4811–900.
13. Schmidt C, et al. Chemical looping approaches to decarbonization via CO<sub>2</sub> repurposing. *Discov Chem Eng*. 2023;3(1):15.
14. Joshi RK, et al. Biogas conversion to liquid fuels via chemical looping single reactor system with CO<sub>2</sub> utilization. *Discov Chem Eng*. 2023;3(1):13.
15. Parkhi A, et al. Carbon dioxide capture from the Kraft mill limekiln: process and techno-economic analysis. *Discov Chem Eng*. 2023;3(1):8.
16. Brewis I, et al. Combining experimental and theoretical insights for reduction of CO<sub>2</sub> to multi-carbon compounds. *Discov Chem Eng*. 2022;2(1):2.
17. Ghomian, Y., K. Sepehrnoori, and G.A. Pope. Efficient Investigation of uncertainties in flood design parameters for coupled CO<sub>2</sub> sequestration and enhanced oil recovery. in SPE International Conference on CO<sub>2</sub> Capture, Storage, and Utilization. 2010.
18. Shah MS, Tsapatsis M, Siepmann JI. Hydrogen sulfide capture: from absorption in polar liquids to oxide, zeolite, and metal-organic framework adsorbents and membranes. *Chem Rev*. 2017;117(14):9755–803.
19. Abdirakhimov M, Al-Rashed MH, Wójcik J. Recent attempts on the removal of H<sub>2</sub>S from various gas mixtures using zeolites and waste-based adsorbents. *Energies*. 2022;15(15):5391.
20. Zwain HM, et al. Modelling of hydrogen sulfide fate and emissions in extended aeration sewage treatment plant using TOXCHEM simulations. *Sci Rep*. 2020;10(1):22209.
21. Poe WA, Mokhatab S. Modeling control, and optimization of natural gas processing plants. Amsterdam: Elsevier; 2016.
22. Farooqi AS, et al. Simulation of natural gas treatment for acid gas removal using the ternary blend of MDEA, AEEA, and NMP. *Sustainability*. 2022;14(17):10815.
23. George EC, Riverol C. Effectiveness of Amine concentration and circulation rate in the CO<sub>2</sub> removal process. *Chem Eng Technol*. 2020;43(5):942–9.
24. Xue J, et al. Research and performance evaluation on selective absorption of H<sub>2</sub>S from gas mixtures by using secondary alkanolamines. *Processes*. 2022;10(9):1795.
25. Nemestóthy N, et al. The impact of various natural gas contaminant exposures on CO<sub>2</sub>/CH<sub>4</sub> separation by a polyimide membrane. *Membranes*. 2020;10(11):324.
26. Rufford TE, et al. The removal of CO<sub>2</sub> and N<sub>2</sub> from natural gas: a review of conventional and emerging process technologies. *J Petrol Sci Eng*. 2012;94–95:123–54.
27. Huertas JI, Giraldo N. Mass Transfer in Chemical Engineering Processes. In: Jozef M, editor. Removal of H<sub>2</sub>S and CO<sub>2</sub> from Biogas by Amine Absorption. Rijeka: IntechOpen; 2011.
28. Adhi TP, et al. H<sub>2</sub>S–CO<sub>2</sub> gas separation with ionic liquids on low ratio of H<sub>2</sub>S/CO<sub>2</sub>. *Heliyon*. 2021;7(12): e08611.
29. Tian G. Applications of green solvents in toxic gases removal green sustainable process for chemical and environmental engineering and. In: Jozef M, editor. Applications of green solvents in toxic gases removal. Amsterdam: Elsevier; 2021.
30. Alqaheem Y. A simulation study for the treatment of Kuwait sour gas by membranes. *Heliyon*. 2021;7(1): e05953.
31. Liu J, et al. Selective H<sub>2</sub>S/CO<sub>2</sub> separation by metal-organic frameworks based on chemical-physical adsorption. *J Phys Chem C*. 2017;121(24):13249–55.

32. Demir H, Keskin S. Computational insights into efficient CO<sub>2</sub> and H<sub>2</sub>S capture through zirconium MOFs. *J CO<sub>2</sub> Utilization*. 2022;55:101811.
33. Liu G, et al. New Technique Integrating Hydrate-Based Gas Separation and Chemical Absorption for the Sweetening of Natural Gas with High H<sub>2</sub>S and CO<sub>2</sub> Contents. *ACS Omega*. 2021;6(40):26180–90.
34. Tasdemir HM, Yasyerli S, Yasyerli N. Selective catalytic oxidation of H<sub>2</sub>S to elemental sulfur over titanium based Ti–Fe, Ti–Cr and Ti–Zr catalysts. *Int J Hydrogen Energy*. 2015;40(32):9989–10001.
35. Khairulin S, et al. Direct selective oxidation of hydrogen sulfide: laboratory, pilot and industrial tests. *Catalysts*. 2021;11(9):1109.
36. Ofori K, et al. An investigation of some H<sub>2</sub>S thermodynamical properties at the water interface under pressurised conditions through molecular dynamics. *Mol Phys*. 2021;120:e2011972.
37. Thibeau, S., J.W. Barker, and D. Morel. Simulation Of Sour Gas Injection Into Low Permeability Oil Reservoirs in SPE Annual Technical Conference and Exhibition. 2003.
38. Luo E, et al. An evaluation on mechanisms of miscibility development in acid gas injection for volatile oil reservoirs. *Oil Gas Sci Technol Rev IFP Energ Nouvelles*. 2019;74:59.
39. Soong Y, et al. Utilization of multiple waste streams for acid gas sequestration and multi-pollutant control. *Chem Eng Technol*. 2012;35(3):473–81.
40. Hassanpouryouzband A, et al. CO<sub>2</sub> capture by injection of flue gas or CO<sub>2</sub>–N<sub>2</sub> mixtures into hydrate reservoirs: dependence of co<sub>2</sub> capture efficiency on gas hydrate reservoir conditions. *Environ Sci Technol*. 2018;52(7):4324–30.
41. Hassanpouryouzband A, et al. Geological CO<sub>2</sub> capture and storage with flue gas hydrate formation in frozen and unfrozen sediments: method development, real time-scale kinetic characteristics, efficiency, and clathrate structural transition. *ACS Sustain Chem Eng*. 2019;7(5):5338–45.
42. Pellegrini LA, De Guido G, Moiosi S. Design of the CO<sub>2</sub> removal section for PSA tail gas treatment in a hydrogen production plant. *Frontiers in Energy Res*. 2020. <https://doi.org/10.3389/fenrg.2020.00077>.
43. Warnecki M, et al. Study of the long term acid gas sequestration process in the borzęcin structure: measurements insight. *Energies*. 2021;14(17):5301.
44. Stephan S, Hasse H. Interfacial properties of binary mixtures of simple fluids and their relation to the phase diagram. *Phys Chem Chem Phys*. 2020;22(22):12544–64.
45. Dawass N, et al. Solubility of carbon dioxide, hydrogen sulfide, methane, and nitrogen in monoethylene glycol; experiments and molecular simulation. *J Chem Eng Data*. 2021;66(1):524–34.
46. Khosravi V, et al. Investigating the applicability of molecular dynamics simulation for estimating the wettability of sandstone hydrocarbon formations. *ACS Omega*. 2020;5(36):22852–60.
47. Seyyedattar M, Zendeheboudi S, Butt S. Molecular dynamics simulations in reservoir analysis of offshore petroleum reserves: a systematic review of theory and applications. *Earth Sci Rev*. 2019;192:194–213.
48. Zhao J, et al. Molecular dynamics simulation of the salinity effect on the n-decane/water/vapor interfacial equilibrium. *Energy Fuels*. 2018;32(11):11080–92.
49. Mecke M, Winkelmann J, Fischer J. Molecular dynamics simulation of the liquid–vapor interface: the lennard-Jones fluid. *J Chem Phys*. 1997;107(21):9264–70.
50. Machel HG. Geological and hydrogeological evaluation of the Nisku Q-Pool in Alberta, Canada, for H<sub>2</sub>S and/or CO<sub>2</sub> Storage. *Oil Gas Sci Technol Rev IFP*. 2005;60(1):51–65.
51. Ofori K, et al. Some interfacial properties of water and co<sub>2</sub>/h<sub>2</sub>s at quasireservoir conditions: a molecular dynamics study. *SPE J*. 2022. <https://doi.org/10.2118/212843-PA>.
52. Hauber, G., Norway's Sleipner and Snøhvit CCS: Industry models or cautionary tales? Institute for Energy Economics and Financial Analysis (IEEFA). 2023. p. 62.
53. Plimpton S. Fast parallel algorithms for short-range molecular dynamics. *J Comp Phys*. 1995;117(1):1–19.
54. Abascal JL, Vega C. A general purpose model for the condensed phases of water: TIP4P/2005. *J Chem Phys*. 2005;123(23): 234505.
55. Harris JG, Yung KH. Carbon dioxide's liquid-vapor coexistence curve and critical properties as predicted by a simple molecular model. *J Chem Phys*. 1995;99:12021.
56. Nath SK. Molecular simulation of vapor–liquid phase equilibria of hydrogen sulfide and its mixtures with alkanes. *J Phys Chem B*. 2003;107(35):9498–504.
57. Cornell WD, et al. A second generation force field for the simulation of proteins, nucleic acids, and organic molecules. *J Am Chem Soc*. 1995;117(19):5179–97.
58. Cardini G. A comparison between the rigid and flexible model of cyclohexane in the plastic phase by molecular dynamic simulations. *Chem Phys*. 1995;193(1):101–8.
59. Nosé S. A molecular dynamics method for simulations in the canonical ensemble. *Mol Phys*. 1984;52(2):255–68.
60. Hoover WG. Canonical dynamics: equilibrium phase-space distributions. *Phys Rev A*. 1985;31(3):1695–7.
61. Allen MP, Tildesley DJ. *Computer simulation of liquids*. Oxford: Clarendon Press; 1987.
62. Ewald PP. Die berechnung optischer und elektrostatischer gitterpotentiale. *Ann Phys*. 1921;369(3):253–87.
63. Hockney RW. *Eastwood computer simulation using particles*. New York: McGraw-Hill International Book; 1981.
64. Ryckaert J-P, Ciccotti G, Berendsen HJC. Numerical integration of the cartesian equations of motion of a system with constraints: molecular dynamics of n-alkanes. *J Comput Phys*. 1977;23(3):327–41.
65. Plimpton S, Crozier P, Thompson A. LAMMPS-large-scale atomic/molecular massively parallel simulator. *Sandia Natl Laboratories*. 2007;18:43.
66. Thermophysical Properties of Fluid Systems. NIST Chemistry WebBook, SRD 69. <https://webbook.nist.gov/chemistry/fluid/>.
67. Kirkwood JG, Buff FP. The statistical mechanical theory of surface tension. *J Chem Phys*. 1949;17(3):338–43.
68. Zhao L, Tao L, Lin S. Molecular dynamics characterizations of the supercritical CO<sub>2</sub>-mediated hexane-brine interface. *Ind Eng Chem Res*. 2015;54(9):2489–96.

69. Liu B, et al. Reduction in interfacial tension of water–oil interface by supercritical CO<sub>2</sub> in enhanced oil recovery processes studied with molecular dynamics simulation. *J Supercritical Fluids*. 2016;111:171–8.
70. Shah V, et al. Water/acid gas interfacial tensions and their impact on acid gas geological storage. *Intl J Greenhouse Gas Control*. 2008;2(4):594–604.
71. Stephan S, et al. Vapor-liquid interfacial properties of the system cyclohexane + CO<sub>2</sub>: experiments, molecular simulation and density gradient theory. *Fluid Phase Equilib*. 2020;518: 112583.
72. Weldon R, Wang F. Simulating a flexible water model as rigid: Best practices and lessons learned. *J Chem Phys*. 2023. <https://doi.org/10.1063/5.0143836>.
73. Tironi IG, Brunne RM, van Gunsteren WF. On the relative merits of flexible versus rigid models for use in computer simulations of molecular liquids. *Chem Phys Lett*. 1996;250(1):19–24.
74. van der Spoel D, van Maaren PJ, Berendsen HJC. A systematic study of water models for molecular simulation: derivation of water models optimized for use with a reaction field. *J Chem Phys*. 1998;108(24):10220–30.
75. Moghadasi R, Rostami A, Hemmati-Sarapardeh A. Chapter three—in fundamentals of enhanced oil and gas recovery from conventional and unconventional reservoirs. In: Bahadori A, editor. *Enhanced Oil Recovery Using CO<sub>2</sub>*. Houston: Gulf Professional Publishing; 2018.
76. Sendner C, et al. Interfacial water at hydrophobic and hydrophilic surfaces: slip, viscosity, and diffusion. *Langmuir*. 2009;25(18):10768–81.
77. El-Mahrab-Robert M, et al. Assessment of oil polarity: comparison of evaluation methods. *Int J Pharm*. 2008;348(1–2):89–94.
78. Phan CM. The surface tension and interfacial composition of water/ethanol mixture. *J Mol Liq*. 2021;342: 117505.
79. Orea P, Duda Y, Alejandre J. Surface tension of a square well fluid. *J Chem Phys*. 2003;118(12):5635–9.
80. Vilarrasa V, Rutqvist J. Thermal effects on geologic carbon storage. *Earth Sci Rev*. 2017;165:245–56.
81. McRee DE. 3—computational techniques, in practical protein crystallography. San Diego: Academic Press; 1999.
82. Bergfreund J, Bertsch P, Fischer P. Effect of the hydrophobic phase on interfacial phenomena of surfactants, proteins, and particles at fluid interfaces. *Curr Opin Colloid Interface Sci*. 2021;56: 101509.

**Publisher's Note** Springer Nature remains neutral with regard to jurisdictional claims in published maps and institutional affiliations.